X_2YZ X = 3d; Y = 4f

X = 1B: Cu
Y = 4A: Tb, Dy, Er
Z = 4B: Sn

Cu_2YIn

Interest in these materials focuses primarily on the occurrence of superconductivity and long-range magnetic order. The compounds containing Ce and Yb are of interest as possible heavy Fermion systems and also from the point of view of valence stability.

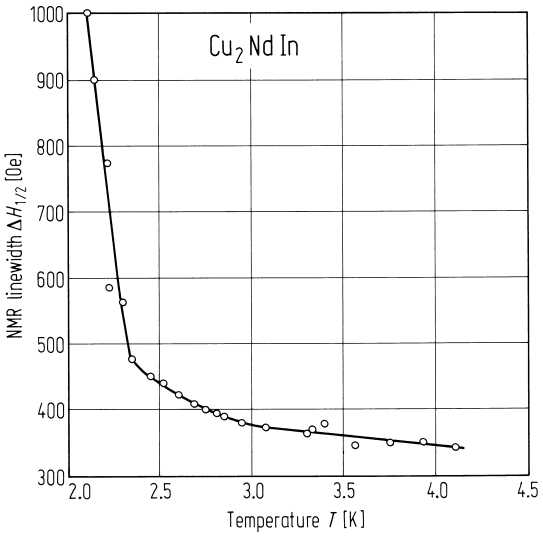

Fig. 468. Temperature dependence of the full linewidth at half maximum height, $\Delta H_{½}$ for the ^{63}Cu NMR spectrum in Cu_2NdIn [90S1].

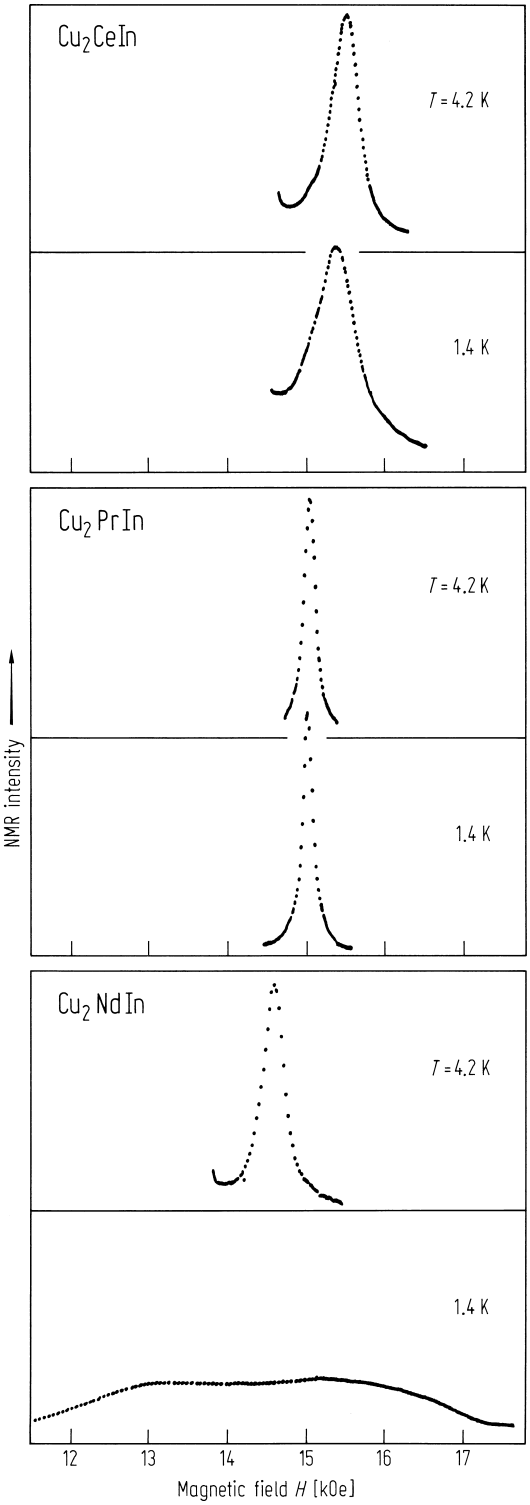

Fig. 467. Field swept ^{63}Cu NMR spectra at 17.0 MHz for Cu_2CeIn, Cu_2PrIn and Cu_2NdIn. For Cu_2NdIn at 1.4 K ^{63}Cu and ^{65}Cu spectra overlap each other [90S1].

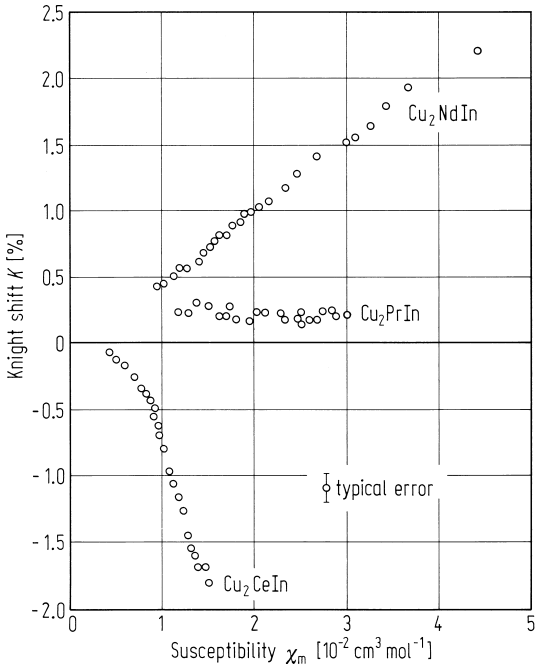

Fig. 469. Knight shift vs. magnetic susceptibility per mole, χ_m, for Cu_2NdIn, Cu_2PrIn and Cu_2CeIn [90S1].

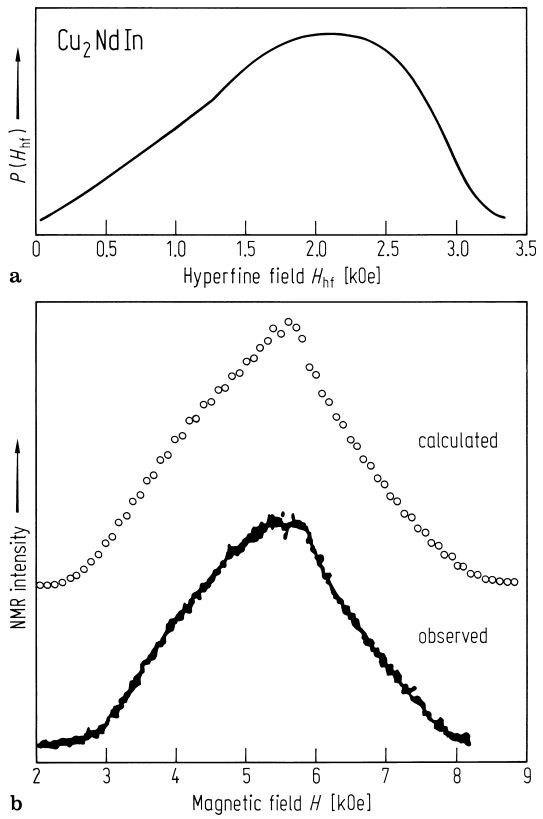

Fig. 470. (**a**) Hyperfine field distribution at Cu site in the antiferromagnetic state of Cu_2NdIn; (**b**) the calculated and observed NMR spectra of ^{63}Cu and ^{65}Cu in Cu_2NdIn at 6.5 MHz [90S1].

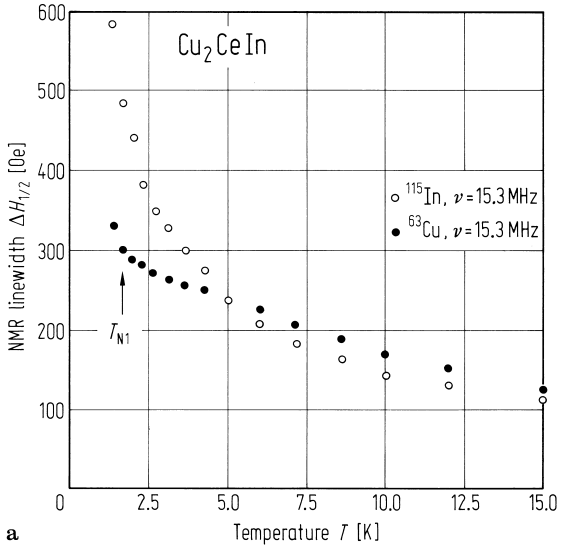

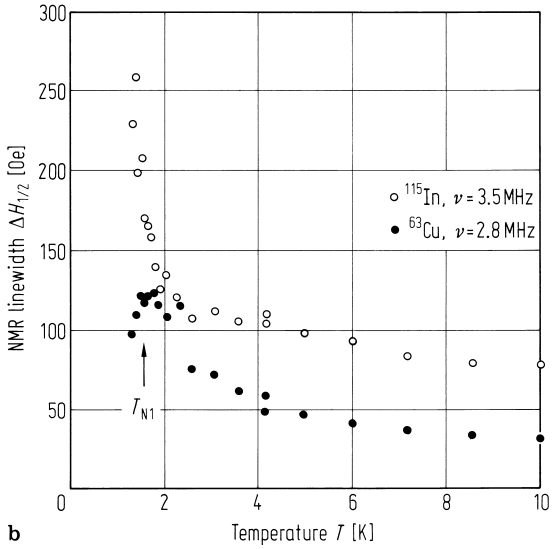

Fig. 472. Temperature dependencies of full width at half maximum for ^{63}Cu and ^{115}In spectra at 15.3 MHz (**a**) and those for ^{63}Cu and ^{115}In spectra at 2.8 and 3.5 MHz (**b**) respectively for Cu_2CeIn [88N1].

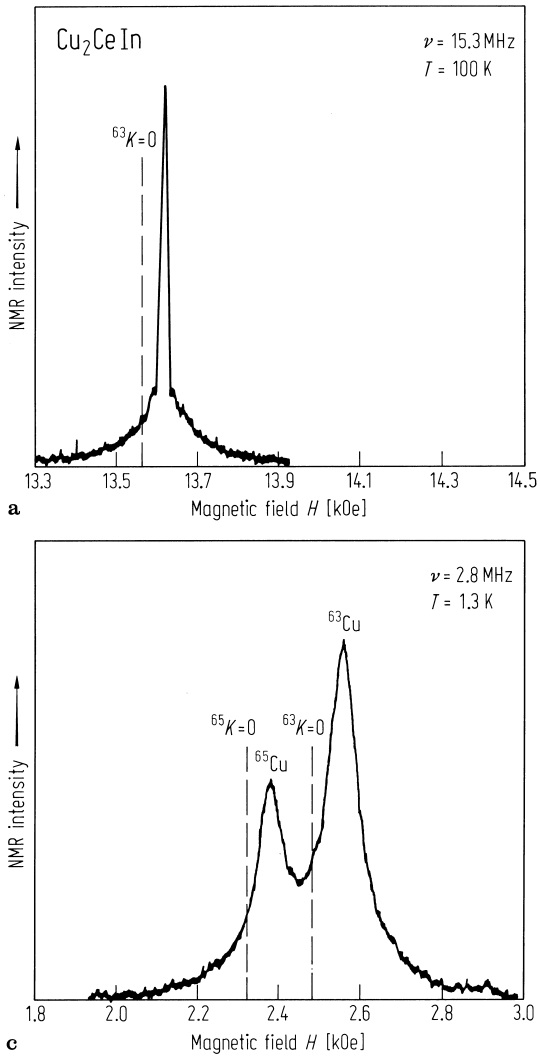

Fig. 471. Cu spin-echo spectra from Cu_2CeIn obtained at (**a**) 100 K and (**b**) 1.3 K for 15.3 MHz and at (**c**) for 2.8 MHz [88N1].

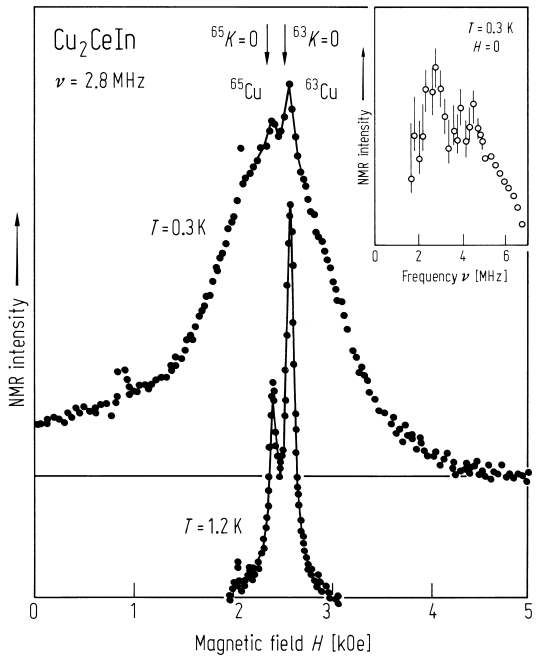

Fig. 473. $^{63,65}Cu$ NMR field swept spectra at 1.2 and 0.3 K from Cu_2CeIn. The insert shows a zero-field Cu NMR spectrum at 0.3 K [88N1].

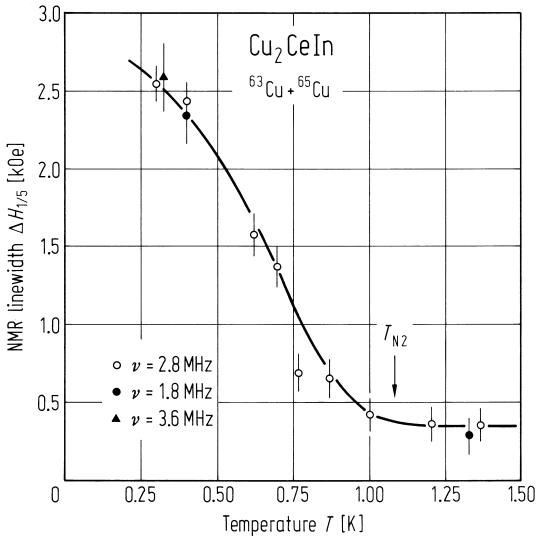

Fig. 474. Temperature dependence of the full width at 1/5 maximum for ^{63,65}Cu spectra [88N1]. T_{N2}: magnetic transition temperature (see Fig. 484).

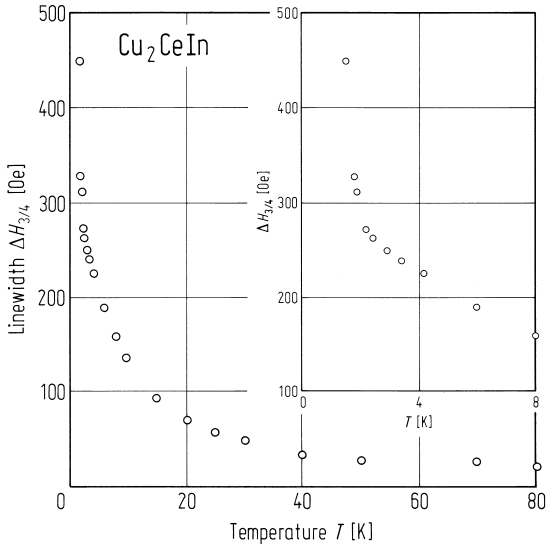

Fig. 476. Temperature dependence of the ^{63}Cu NMR linewidth $\Delta H_{¾}$ for Cu_2CeIn, taken at the resonance frequency of 10.25 MHz, where $\Delta H_{3/4}$ is the full width at three-quarters maximum of the inhomogenously broadened spectrum. The inset shows the lower-temperature part of the figure [88T1].

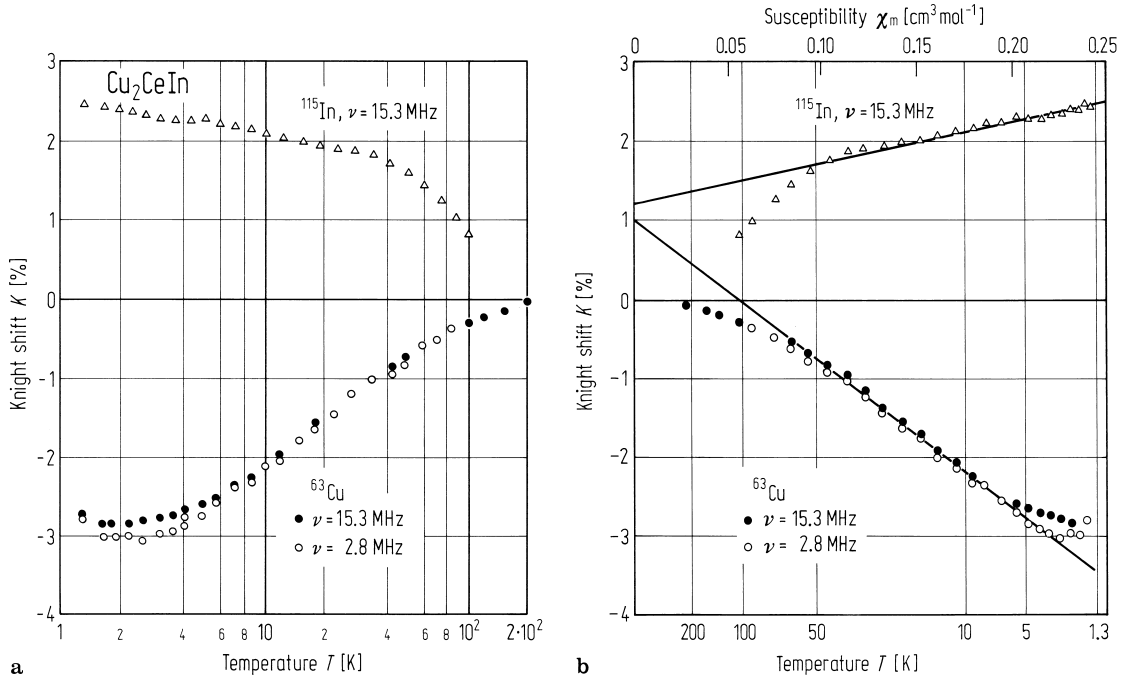

Fig. 475. (**a**) Temperature dependence of the Knight shift for ^{63}Cu and ^{115}In; (**b**) Knight shift vs. susceptibility plots for ^{63}Cu and ^{115}In [88N1].

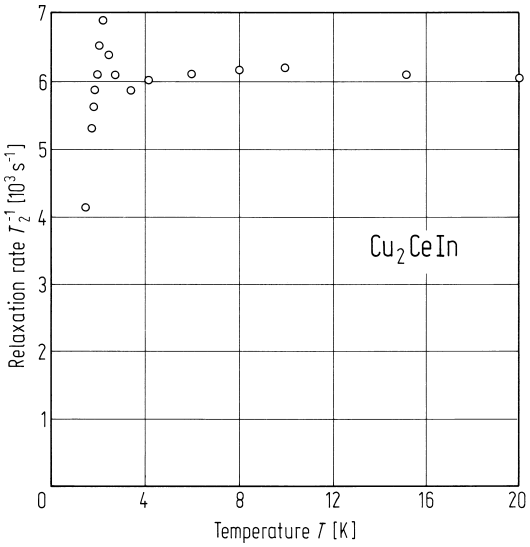

Fig. 477. Temperature dependence of the effective nuclear transverse relaxation rate T_2^{-1} for Cu_2CeIn [88T1].

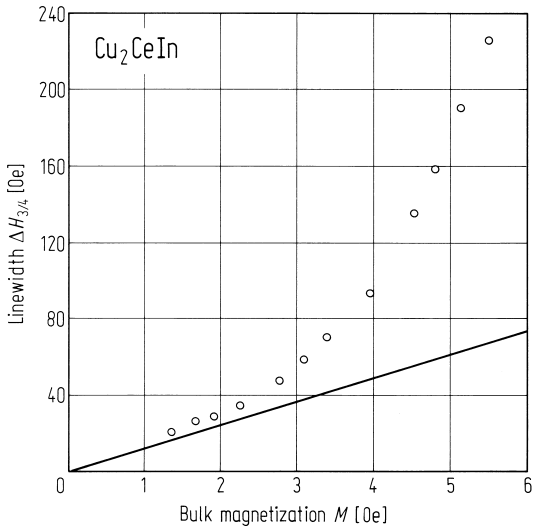

Fig. 478. ^{63}Cu NMR linewidth $\Delta H_{¾}$ for Cu_2CeIn vs. bulk magnetisation M plot with temperature as the implicit parameter between 4.2 and 80 K. The solid line represents the relation $\Delta H_{¾} = 4\pi M$, where the factor 4π corresponds to the distribution of demagnetising factors in a powdered specimen [88T1].

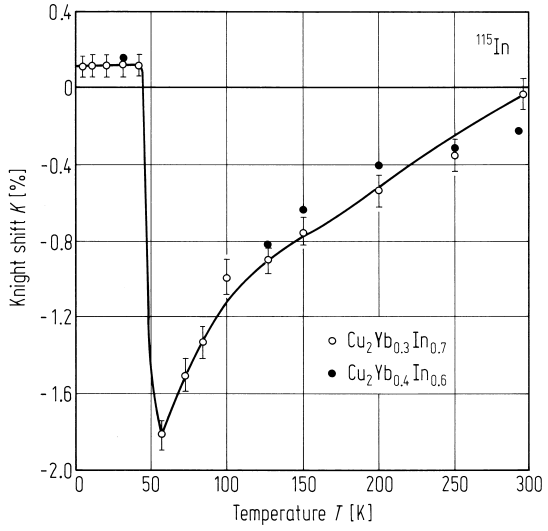

Fig. 479. ^{115}In NMR Knight shift (with respect to $In_2(SO_4)_3$) as a function of temperature of $Cu_2Yb_xIn_{1-x}$. x = 0.3, 0.4 [87S1].

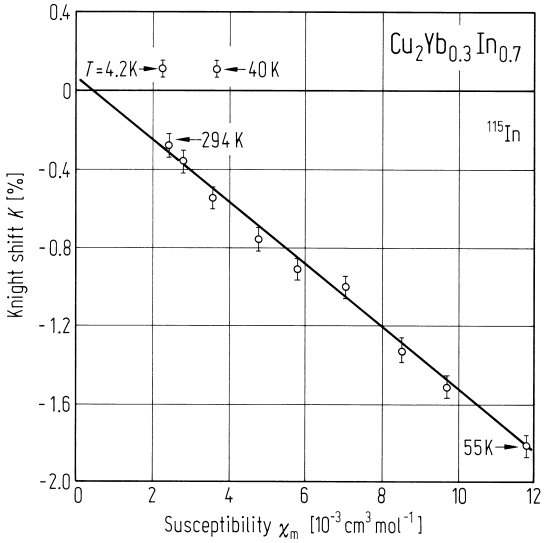

Fig. 480. The plot of ^{115}In NMR Knight shift vs. susceptibility (with temperature as an implicit parameter) for $Cu_2Yb_{0.3}In_{0.7}$ [87S1].

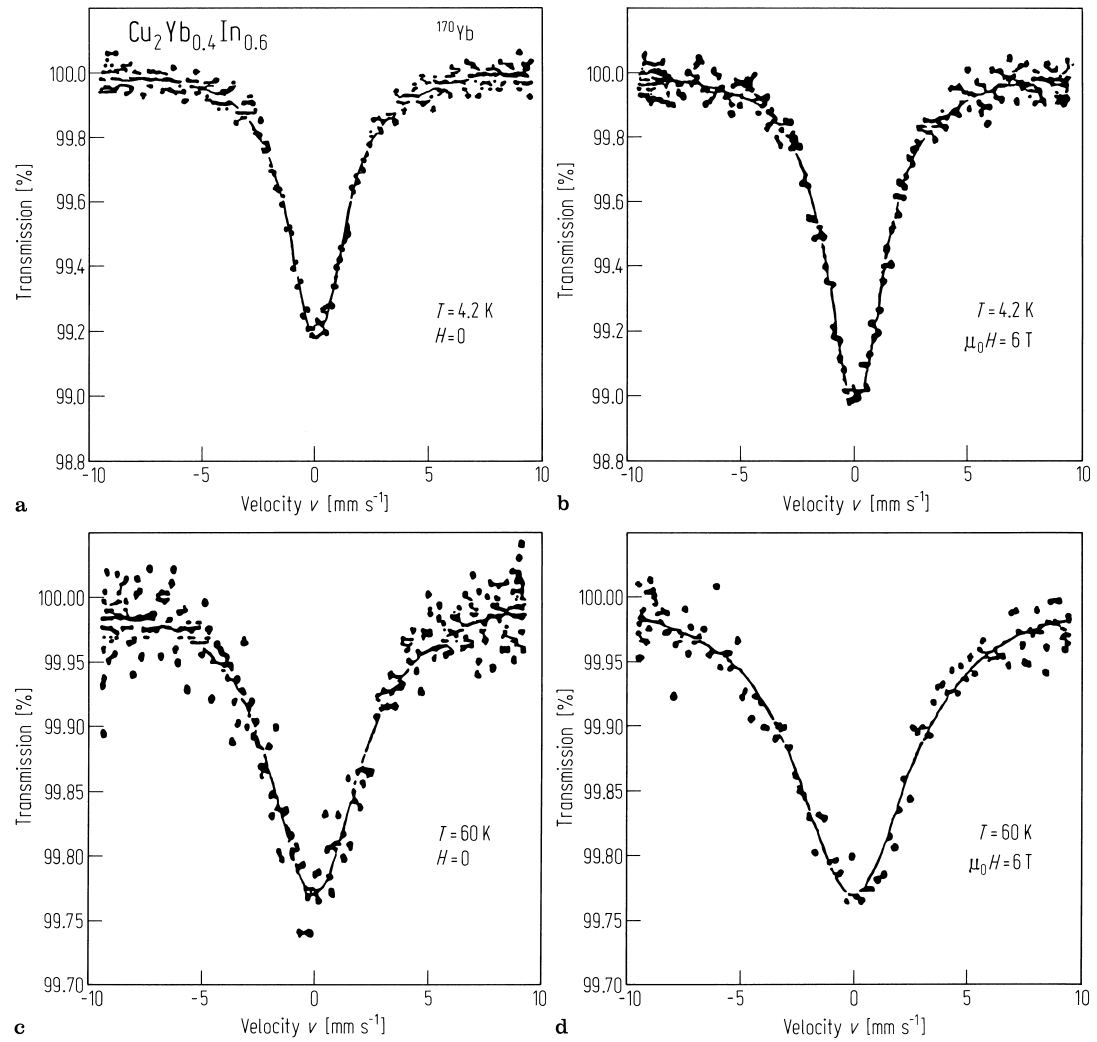

Fig. 481. Mössbauer spectra of the 84-keV transition of ^{170}Yb in $Cu_2Yb_{0.4}In_{0.6}$ [87F1].

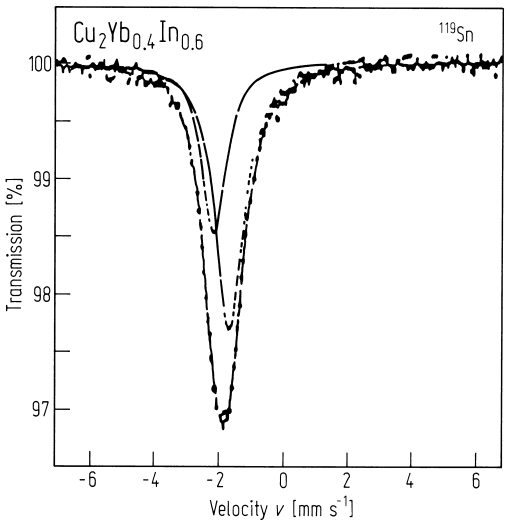

Fig. 482. A typical Mössbauer spectrum of the 24-keV hyperfine transition of ^{119}Sn in $Cu_2Yb_{0.4}In_{0.6}$ [87F1].

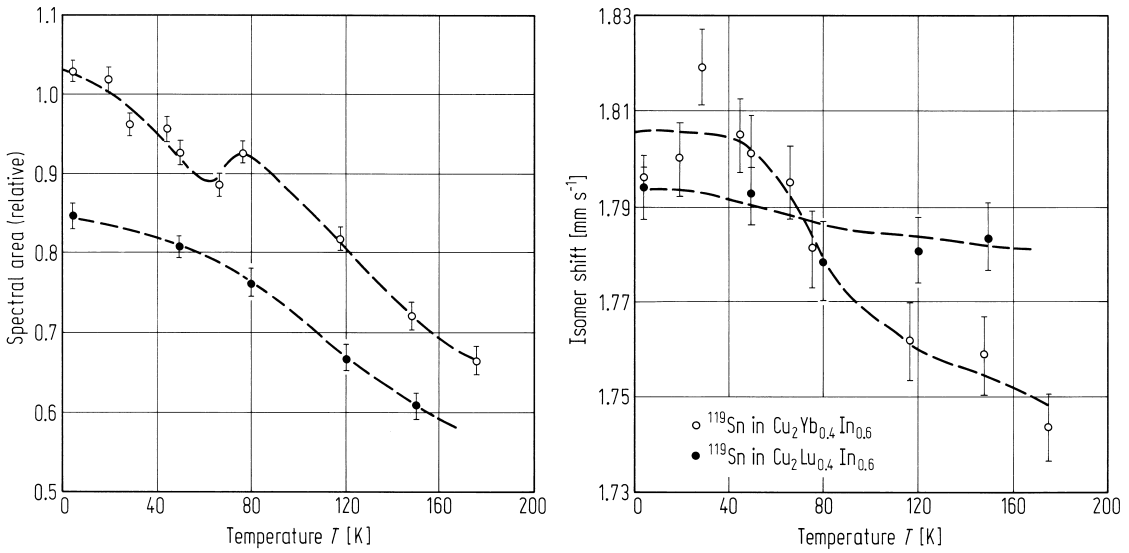

Fig. 483. Temperature dependence of the spectral area and average isomer shift of the Mössbauer spectra of ^{119}Sn in $Cu_2Yb_{0.4}In_{0.6}$ and $Cu_2Lu_{0.4}In_{0.6}$ [87F1].

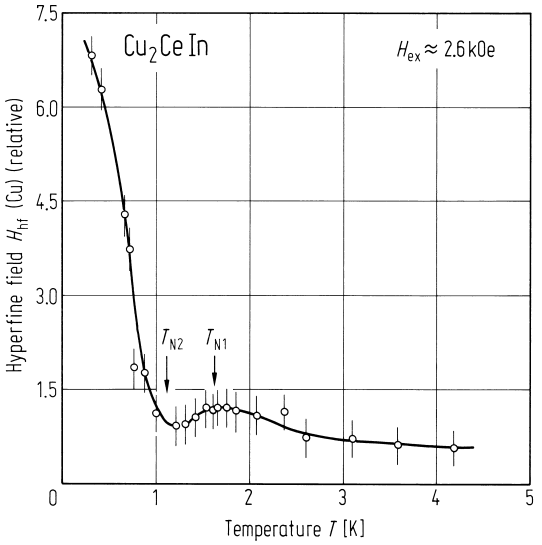

Fig. 484. Temperature dependence of the hyperfine field at the Cu site in $Cu_2Ce_{1.03}In$ evaluated from field swept Cu NMR spectra at 2.8 MHz. The results suggest two magnetic transitions at T_{N1} = 1.6 and T_{N2} = 1.1 K [88N2].

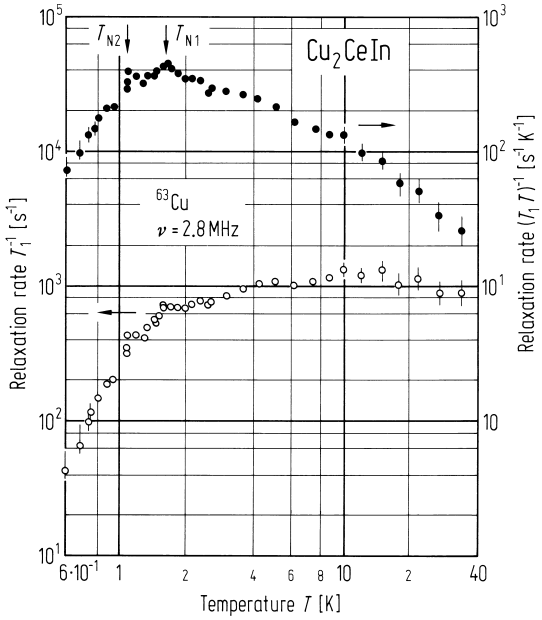

Fig. 485. Temperature dependence of $1/T_1$ (open circles) and $1/T_1T$ (solid circles) of ^{63}Cu in $Cu_2Ce_{1.03}In$ measured at 2.8 MHz [88N2].

X_2YZ X = 4d; Y = 4f

X = 8A: Pd
Y = 4A: Tb, Dy, Er
Z = 4B: Sn

Pd_2YSn

All three compounds order magnetically with the Er compound reported to be simultaneously magnetic and superconducting.

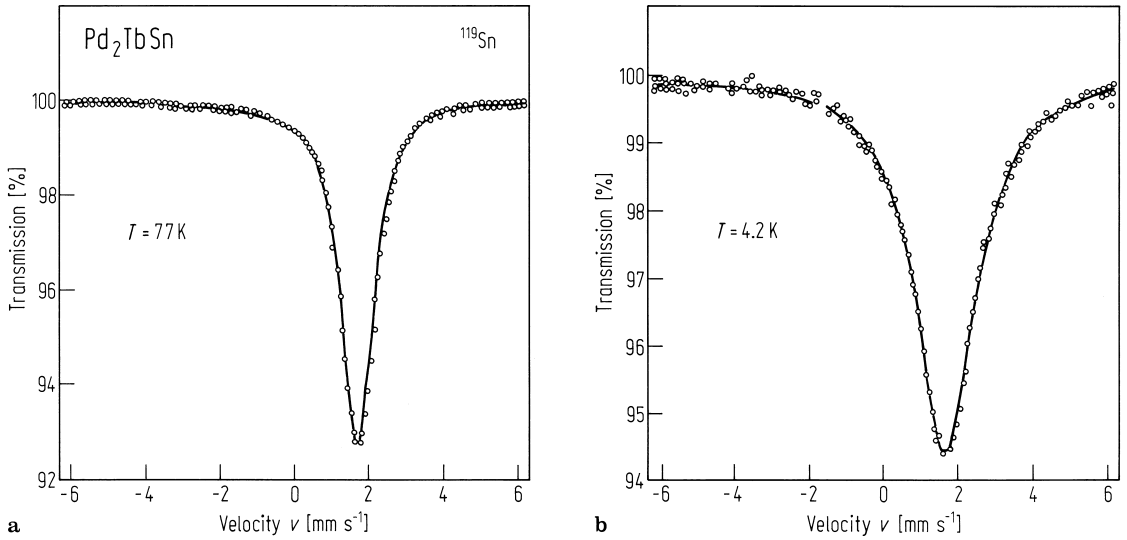

Fig. 486. ^{119}Sn Mössbauer spectra of Pd_2TbSn at (**a**) 77 K and (**b**) 4.2 K [85M1].

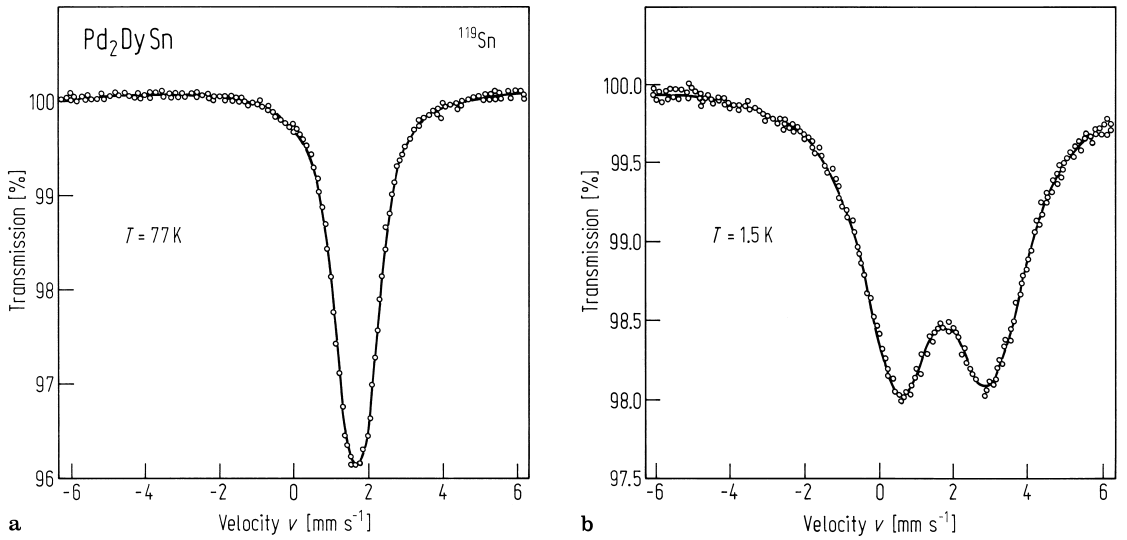

Fig. 487. ^{119}Sn Mössbauer spectra of Pd_2DySn at (**a**) 77 K and (**b**) below the Néel temperature at 1.5 K. At 1.5 K the field at the Sn site is estimated to be 5 T [85M1].

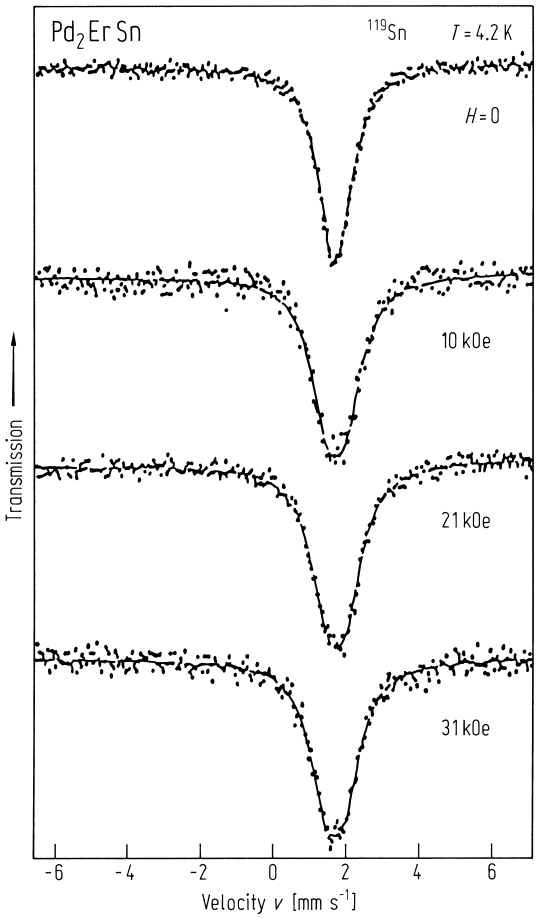

Fig. 488. ^{119}Sn Mössbauer spectra of Pd_2ErSn at 4.2 K. The externally applied fields H are 0, 10 kOe, 21 kOe and 31 kOe [87S2].

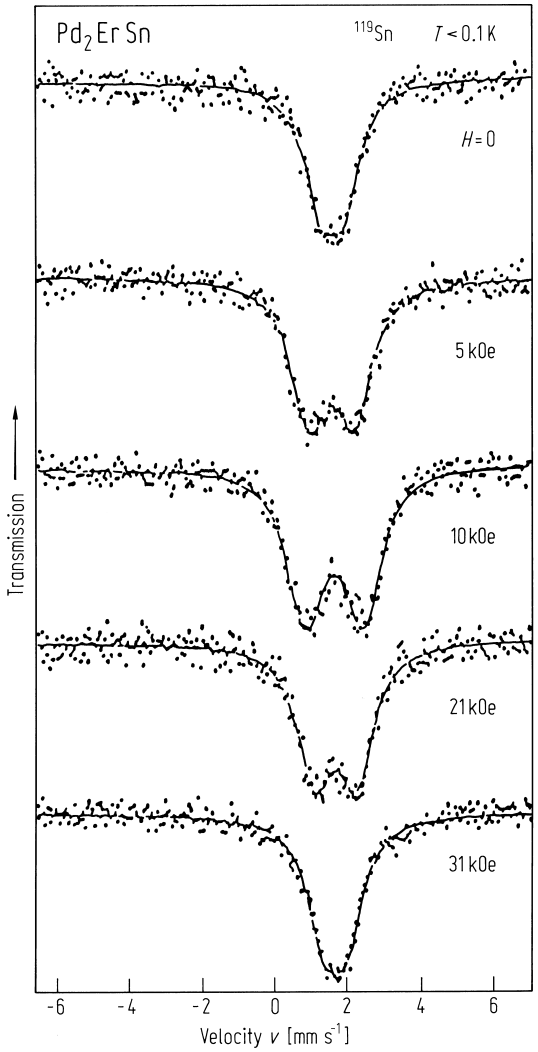

Fig. 489. ^{119}Sn Mössbauer spectra of Pd_2ErSn at $T < 0.1$ K and H = 0, 5 kOe, 10 kOe, 21 kOe and 31 kOe [87S2].

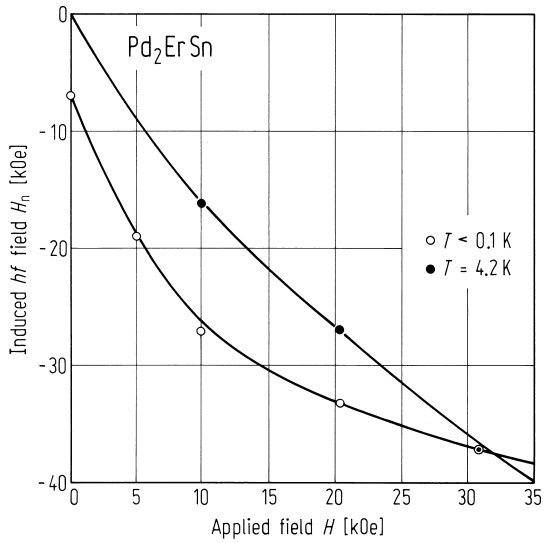

Fig. 490. Induced hyperfine fields H_n at a Sn site in Pd_2ErSn at 4.2 K and below 0.1 K as a function of external field [87S2].

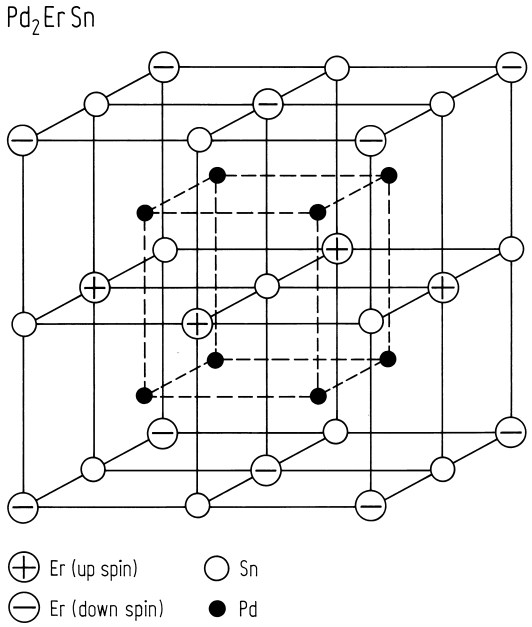

Fig. 491. Local atomic arrangement around an Sn site in Pd_2ErSn. + and – indicate probable spin directions [87S2].

Films

X_2YZ X = 3d ; Y = 3d

X = 1B: Cu
Y = 7A: Mn
Z = 3B: Al

Cu_2MnAl

NMR spin echo measurements have been carried out on sputtered Cu_2MnAl films grown with different substrate temperatures between 50 °C and 300 °C.

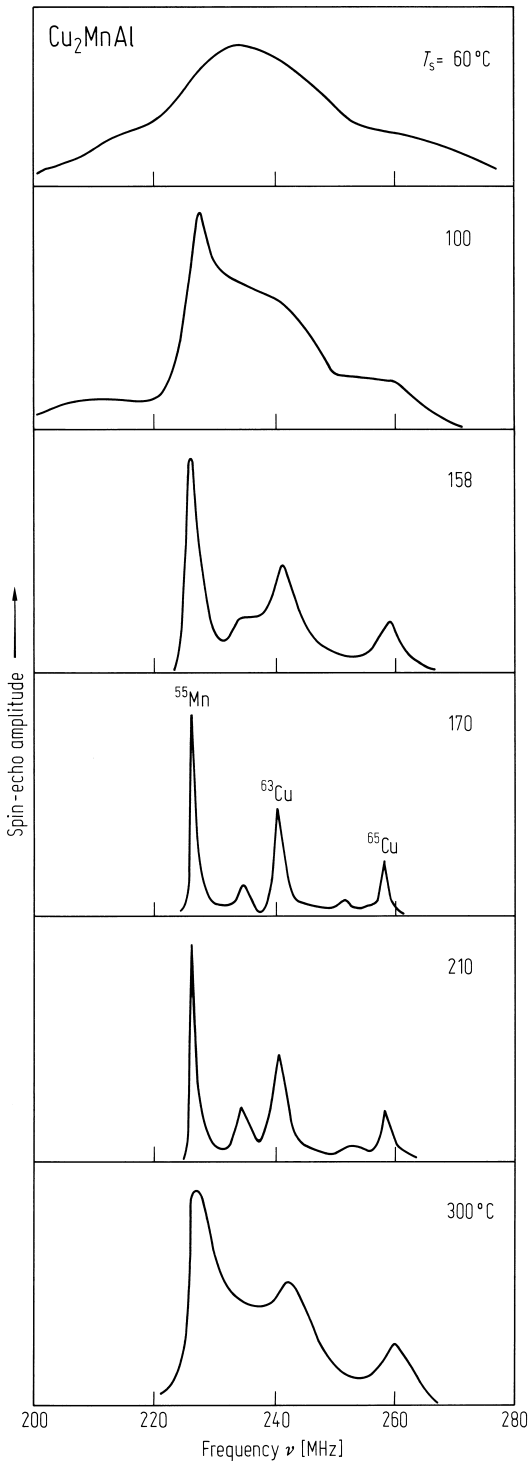

Fig. 492. ^{55}Mn, ^{63}Cu and ^{65}Cu NMR spin echo at 4.2 K in sputtered Cu_2MnAl films deposited at various substrate temperatures T_s. The residual lines between the main lines are due to deviations from exact stoichiometry [88L1].

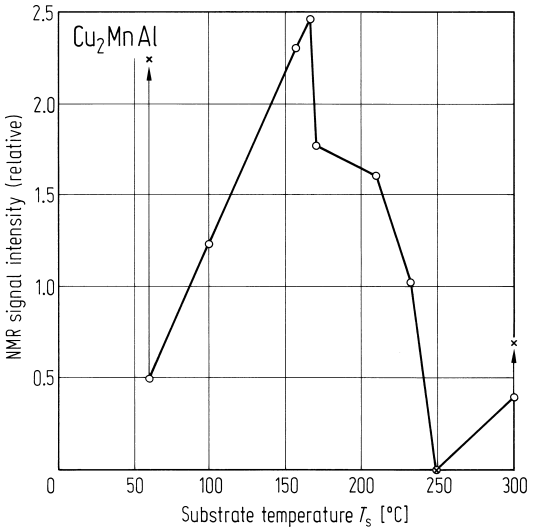

Fig. 493. Integrated signal intensity as a function of substrate temperature for Cu_2MnAl films. The symbol × refers to samples annealed at 160 °C for 4 h [88L1].

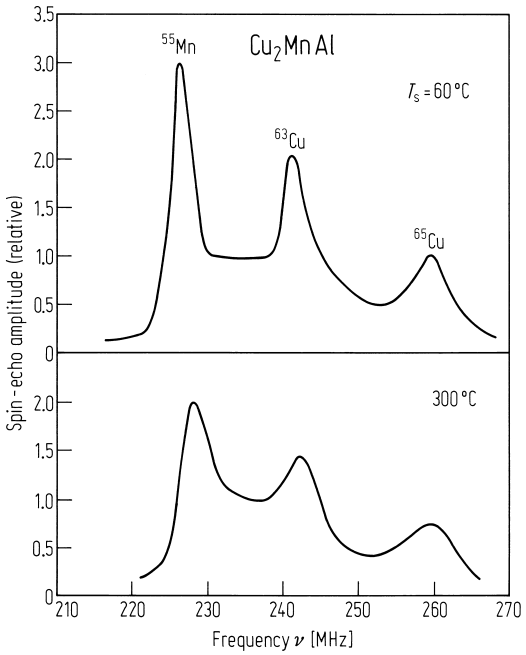

Fig. 494. NMR spin echo spectra at 4.2 K for Cu_2MnAl alloy films deposited at T_s = 60 °C and 300 °C after annealing at 160 °C [88L1].

$C1_bXYZ$ X = 3d, 4d, 5d; Y = 3d

X = 8A: Ni, Rh, Ir, Pt; 1B: Au
Y = 7A: Mn
Z = 4B: Sn ; 5B: Sb

Interest in the $C1_b$ compounds is focused on the predicted half-metallic ferromagnetic properties.

Table 102. Resonance frequencies and hyperfine fields on ^{55}Mn and ^{121}Sb in some Ni-Mn-Sb alloys [90S2].

Composition	ν (^{55}Mn) [MHz]	H (^{55}Mn) [kOe]	ν (^{121}Sb) [MHz]	H (^{121}Sb) [kOe]
$Ni_{34.3}Mn_{30.8}Sb_{34.9}$	299.7	– 283.8	302.5	297.2
$Ni_{34.8}Mn_{29.3}Sb_{35.9}$	299.9	– 284.0	304.1	299.2
$Ni_{34.2}Mn_{28.9}Sb_{36.9}$	299.7	– 283.8	305.4	300.5

Table 103. Environment of different crystallographic sites in the six nearest neighbour shells in the $C1_b$ structure. *V* denotes empty sites [90S2].

Site	I	II	III	IV	V	VI
V	4 Mn + 4 Sb	6 Ni	12 *V*	12 Mn + 12 Sb	8 Ni	6 *V*
Ni	4 Mn + 4 Sb	6 *V*	12 Ni	12 Mn + 12 Sb	8 *V*	6 Ni
Mn	4 Ni + 4 *V*	6 Sb	12 Mn	12 Ni + 12 *V*	8 Sb	6 Mn
Sb	4 Ni + 4 *V*	6 Mn	12 Sb	12 Ni + 12 *V*	8 Mn	6 Sb

Table 104. Measured hyperfine fields at sp sites in $C1_b$ alloys, together with structural and magnetic data [83D1]. (a) Pd site, (b) Mn site, (c) Sb site.

Host	*a* [Å]	*p* [μ_B]	T_C [K]	Probe	*H* [kOe]	*T* [K]
NiMnSb	5.913	3.8	720	Cd	+ 213(3)	77
				Cd	– 211(4)	95
				Sn	53(5)	77
				Sb	+ 276(5)	77
$Rh_{0.98}Mn_{1.04}Sb_{0.98}$	6.152	3.63	320	Cd	35(10)	300
				Cd	– 95(10)	77
				Sb	116(5)	77
PdMnSb	6.264	3.95	500	Cd (a)	– 150	0
				Cd (b)	+ 250	0
				Cd (c)	– 250	0
				Cd	273(8)	77
				Sn	+ 103	77
				Sb	+ 329(5)	78
				Te	+ 568	4.2
				I	+ 681	4.2
$Ir_{1.07}Mn_{1.07}Sn_{0.86}$	6.199	2.25	204	Cd	– 108(4)	77
				Sn	+ 30	77
$Ir_{0.92}Mn_{1.16}Sb_{0.92}$	6.164	3.1	290	Cd	69(5)	273
				Cd	166(5)	77
				Sb	+ 65(5)	77
PtMnGa	6.15	3.18	220	Cd	196(9)	77
PtMnSn	6.269	3.54	330	Cd	+ 95	77
				Sn	– 30	77
PtMnSb	6.195	4.02	575	Cd	+ 161(1)	77
				Cd	166(4)	77
				Sn	62(5)	77
				Sb	+ 210(5)	77
AuMnSb	6.373	2.21	72	Sb	+ 410	4.2

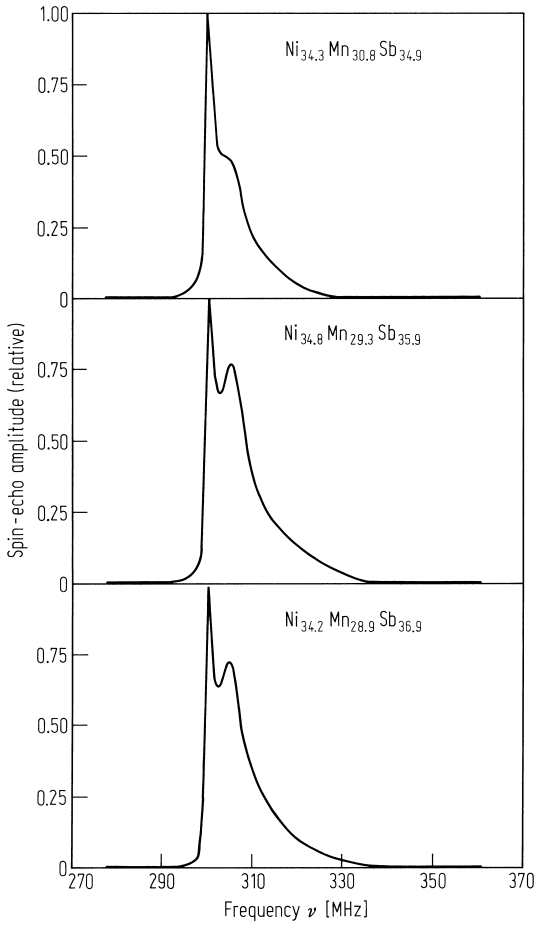

Fig. 495. Spin echo spectra of $Ni_{34.3}Mn_{30.8}Sb_{34.9}$, $Ni_{34.8}Mn_{29.3}Sb_{35.9}$ and $Ni_{34.2}Mn_{28.9}Sb_{36.9}$ [90S2].

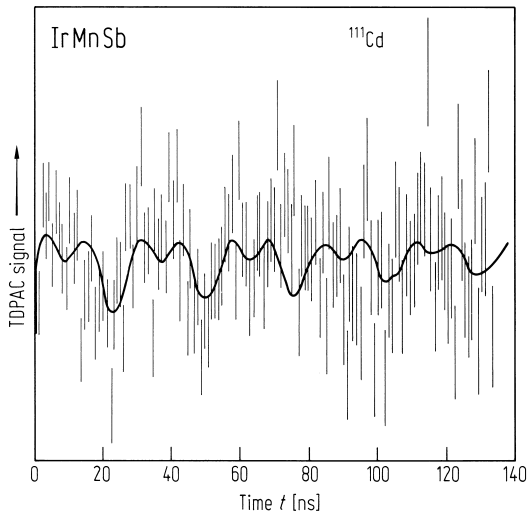

Fig. 496. TDPAC spectrum for ^{111}Cd in IrMnSb at 77 K [83D1].

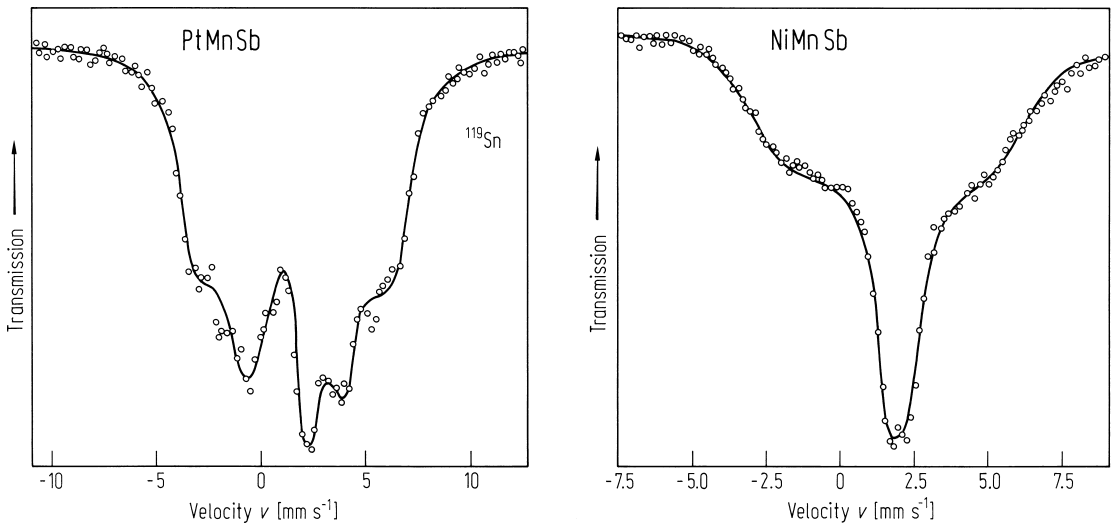

Fig. 497. ^{119}Sn Mössbauer spectra in PtMnSb and NiMnSb at 77 K [83D1].